A Chemically Orthogonal Hole Transport Layer for Efficient Colloidal Quantum Dot Solar Cells

Margherita Biondi, Min-Jae Choi, Olivier Ouellette, Se-Woong Baek, Petar Todorović, Bin Sun, Seungjin Lee, Mingyang Wei, Peicheng Li, Ahmad R. Kirmani, Laxmi K. Sagar, Lee J. Richter, Sjoerd Hoogland, Zheng-Hong Lu, F. Pelayo García de Arquer, and Edward H. Sargent*

Colloidal quantum dots (CQDs) are of interest in light of their solution-processing and bandgap tuning. Advances in the performance of CQD optoelectronic devices require fine control over the properties of each layer in the device materials stack. This is particularly challenging in the present best CQD solar cells, since these employ a p-type hole-transport layer (HTL) implemented using 1,2-ethanedithiol (EDT) ligand exchange on top of the CQD active layer. It is established that the high reactivity of EDT causes a severe chemical modification to the active layer that deteriorates charge extraction. By combining elemental mapping with the spatial charge collection efficiency in CQD solar cells, the key materials interface dominating the subpar performance of prior CQD PV devices is demonstrated. This motivates to develop a chemically orthogonal HTL that consists of malonic-acid-crosslinked CQDs. The new crosslinking strategy preserves the surface chemistry of the active layer beneath, and at the same time provides the needed efficient charge extraction. The new HTL enables a 1.4× increase in charge carrier diffusion length in the active layer; and as a result leads to an improvement in power conversion efficiency to 13.0% compared to EDT standard cells (12.2%).

Colloidal quantum dots (CQDs) are of interest in light-emitting diodes,[1,2] lasers,[3] photodetectors,[4] and solar cells[5–14] owing to their tunable optical and electrical properties and their solution processing.[15–18] Research efforts on surface

M. Biondi, Dr. M.-J. Choi, Dr. O. Ouellette, Dr. S.-W. Baek, P. Todorović, Dr. B. Sun, Dr. S. Lee, M. Wei, Dr. L. K. Sagar, Dr. S. Hoogland, Dr. F. P. García de Arquer, Prof. E. H. Sargent
Department of Electrical and Computer Engineering
University of Toronto
10 King's College Road, Toronto, Ontario M5S 3G4, Canada
E-mail: ted.sargent@utoronto.ca
P. Li, Prof. Z.-H. Lu
Department of Material Science and Engineering
University of Toronto
184 College St, Toronto, Ontario M5S 3E4, Canada
Dr. A. R. Kirmani, Dr. L. J. Richter
Materials Science and Engineering Division
National Institute of Standards and Technology (NIST)
Gaithersburg, MD 20899, USA

passivation and device architecture have led to improvements in CQD solar cell performance,[19–21] and these recently enabled power conversion efficiencies (PCE) above 12% for lead sulfide (PbS) CQDs.[19]

The conventional CQD solar cell architecture consists of a transparent cathode, electron transport layer (ETL), a light-absorbing active layer, a hole transport layer (HTL), and a metal anode. To achieve high-performing devices, the optoelectronic properties of the ETL, HTL, and active layer, which determine the charge absorption and extraction capacity of the devices, require accurate control. A number of excellent studies have illuminated the role of the ETL[22–28] and the active layer;[29] while the HTL is relatively less examined. Organic p-type semiconductors[30,31] and metal oxides (e.g., MoO_3, NiO_x, etc.)[32] have been explored to replace the thiol-passivated CQD HTL. Non-thiol ligands (e.g., NaHS)[33,34] have also been reported to produce p-type CQD solids; however, to date, device performance has not yet surpassed that of thiol-passivated CQD-based HTLs.

State-of-art CQD solar cells employ 1,2-ethanedithiol (EDT) in the process of fabricating the CQD HTL.[19] This EDT HTL has been used in most high-performing CQD solar cells; but EDT has long been suspected of negatively affecting the underlying CQD active layer. In particular, its high reactivity[35] is proposed to be implicated in interfering with efficient charge extraction at the back-junction.[36]

Herein we seek experimental evidence of any role of the EDT HTL in performance; and we find, using a new spatial collection efficiency (SCE) technique,[37] that the EDT HTL does indeed cause a rapid drop in the collection efficiency at the interface between HTL and active layer. We then develop an orthogonal CQD HTL that employs malonic acid (MA) instead of EDT. As a result of the lower reactivity of carboxylic acids compared to thiols,[38] the MA HTL substantially preserves the original surface chemistry of the CQD active layer after its deposition, as evidenced by X-ray photoelectron spectroscopy (XPS) analyses.

The orthogonality of the MA HTL enables full charge collection at the back interface in CQD solar cells. This advance
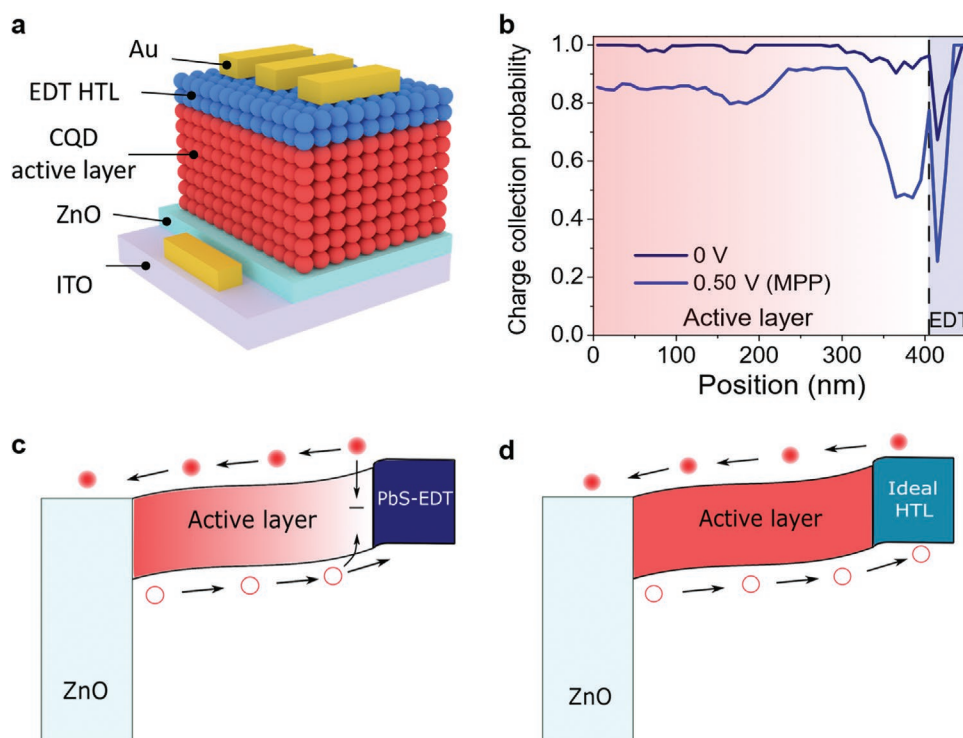
**ADVANCED
SCIENCE NEWS**

www.advancedsciencenews.com

**ADVANCED
MATERIALS**

www.advmat.de

Figure 1. a) CQD solar cell device architecture. b) Calculated charge collection probability versus position in the device for a device with EDT HTL at 0 V and MPP (0.50 V). c) Spatial band diagram for a standard EDT HTL device showing interface recombination at the active layer/HTL interface. d) Spatial band diagram of a full device for the case of an ideal HTL with suppressed interface recombination.

leads to a 1.4× increase in carrier diffusion length in the active layer. As a result, we achieve significant improvements in both fill factor (FF) and short-circuit current density (J_{SC}) compared to the devices with EDT HTLs, resulting in a PCE of 13.0% (12.2% for EDT control devices).

The SCE reports the probability with which charge carriers generated within the device are collected at the electrodes and contribute to the output current (see Experimental Section for details).[37,39] In the best prior PbS CQD solar cell architecture (**Figure 1**a), we observe a low collection efficiency for photocarriers generated near the interface between the active layer and the EDT HTL (Figure 1b, obtained from the internal quantum efficiency (IQE) and photogeneration probability in Figure S1, Supporting Information). At 0 V, the SCE drops sharply to 70% at the interface between the active layer and the HTL. At the maximum power point (MPP), the loss in collection at the interface becomes even more pronounced, dropping to below 50%. The SCE profiles indicate that the EDT HTL results in performance-limiting recombination at its interface with the active layer (Figure 1c).

In light of these findings, we reasoned that an HTL should be sought that minimizes carrier recombination at the interface and offers the needed sufficient conductivity and favorable band alignment (Figure 1d).

To investigate further the mechanistic origins of the rapid drop in charge collection efficiency at the interface between the active layer and the EDT HTL, we reviewed the fabrication process (**Figure 2**a), noting that the solid-state ligand-exchange (deposition of oleic acid (OA)-capped CQDs followed by soaking

with a solution of EDT in acetonitrile and rinsing with acetonitrile) exposes the underlying CQD active layer to thiol ligands during the HTL fabrication step. Since previous studies reported that acetonitrile does not modify the CQDs surface,[40] we note that thiols may penetrate and modify the surface chemistry of the active layer given their high reactivity with the CQD surface.[35]

To challenge this hypothesis, we studied the surface chemistry variation in the CQD active layer following soaking of the active layer directly with EDT solution treatment using XPS (Figure 2b and Figure S2, Supporting Information). The S atomic ratio (signal of the EDT ligand) increases by 50%, whereas the atomic ratio of iodide (signal of the active layer ligand) decreases by 25%. This suggests that EDT ligands substitute the original ligands (PbI_2) of the active layer (Figure 2c), resulting in a drop of charge collection efficiency at the interface.

We sought therefore to find a new HTL ligand that does not interfere with the surface chemistry of the CQD active layer. We turned our attention to carboxylic acid, which has a lower binding strength to metal atoms compared to thiols.[38] We surveyed bidentate carboxylic acid ligands with different lengths of carbon chains to fabricate ligand-exchanged CQD films (Figure S3, Supporting Information). UV–vis absorbance spectra reveal that the first excitonic peak of CQD films exchanged with oxalic acid (OXA, two-carbon chain) is diminished, whereas CQD films exchanged with MA (three-carbon chain) retain a well-defined exciton. We offer that the lower pK_a of OXA compared to MA may lead to CQD aggregation during ligand exchange. Other bidentate carboxylic acid ligands with more than four carbon atoms failed as a result of their low solubility.
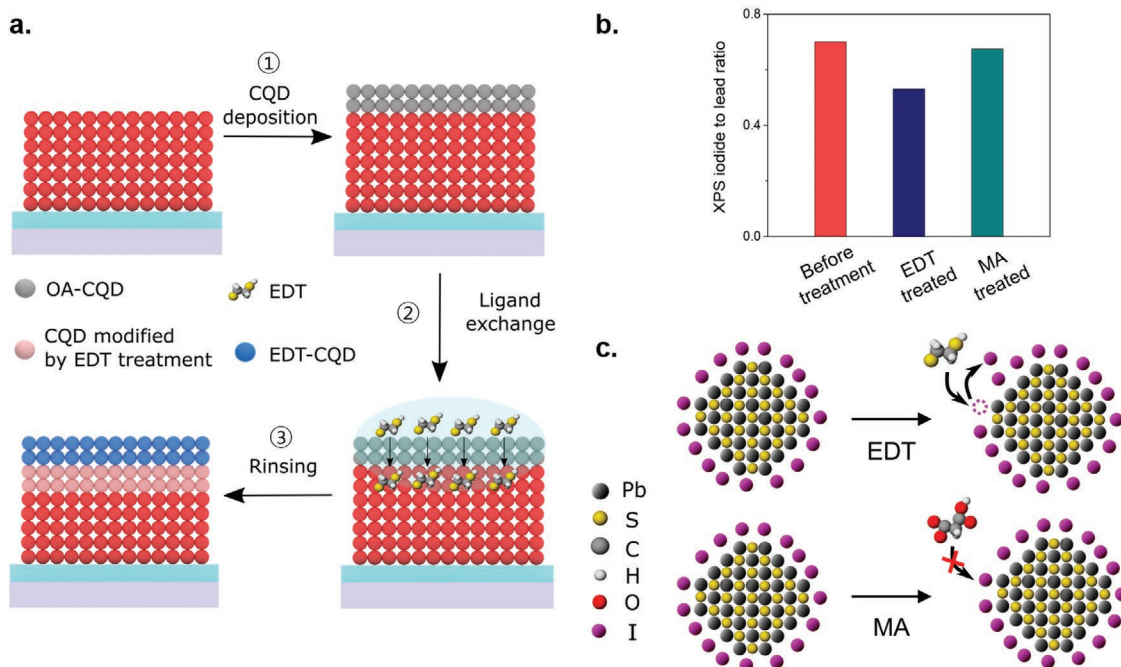
Figure 2. a) Schematic of the EDT HTL fabrication procedure. Process 1: deposition of oleic acid capped CQDs on the CQD active layer. Process 2: soaking of the oleic acid capped CQD film with EDT solution. Process 3: rinsing of the film with acetonitrile. b) Iodide-to-lead ratio from XPS measurement for a bare active layer (before HTL treatment) and after treatment with EDT and MA solution on the active layer. c) Schematic of the proposed mechanism of the consequence of EDT and MA treatment on the CQD of the active layer.

Based on these results, we studied the impact of MA on the active layer surface chemistry using the same XPS studies as previously (Figure 2b). When the active layer is soaked with MA, it retains almost completely the original elemental composition, indicating that MA ligands do not change the surface chemistry of the CQD active layer (Figure 2c).

We then explored whether MA-exchanged CQD films are suitable HTLs for CQD solar cells. Fourier-transform infrared spectroscopy (FTIR) reveals that the characteristic CH symmetric and asymmetric stretching peaks between 3000 and 2800 cm^{-1}, which are visible in the OA-capped CQD film,[41] are completely removed in the MA-exchanged CQD film, indicating complete ligand exchange from OA to MA (**Figure 3**a). The COO$^-$ peak at 1540 cm^{-1}[38] confirms the attachment of MA to the surface of CQDs.

To analyze the band alignment in devices, we performed ultraviolet photoelectron spectroscopy (UPS) of the active layer, EDT HTL, and MA HTL, and then calculated Fermi level (E_F), valence band maximum (VBM) and conduction band minimum (CBM),[42] as summarized in Figure 3b (full UPS spectra shown in Figure S4, Supporting Information). The CBM was estimated from the VBM and the optical bandgap measured by UV–vis absorbance (Figure S5, Supporting Information). The MA HTL has a 0.2 eV deeper E_F compared to the active layer, whereas the EDT HTL has a 0.1 eV shallower E_F. This enables, for the MA HTL, a more favorable band-bending with the active layer, allowing efficient blocking of electrons and extraction of holes from the active layer.

Next we studied interdot spacing using grazing-incidence small-angle X-ray scattering (GISAXS). The results show

that the interdot-spacing between CQDs decreases from 5.5 to 3.0 nm after ligand exchange with MA, whereas the EDT-exchanged CQD film exhibits an interdot-spacing of 3.2 nm (Figure 3c; Figure S7, Supporting Information). As a consequence of this denser packing of MA-exchanged films compared to EDT-exchanged films, the electrical conductivity increases by 1.2× in MA-exchanged films compared to EDT-exchanged films ((1.2 ± 0.1) × 10^{-3} S m^{-1} for EDT films and (1.4 ± 0.05) × 10^{-3} S m^{-1} for MA films, Figure 3d). We also performed mobility measurements using the space charge limited current method; MA PbS CQDs exhibit a mobility of 1 × 10^{-4} cm^2 V^{-1} s^{-1}, while EDT PbS CQDs have a mobility of 0.7 × 10^{-4} (Figure S8, Supporting Information).

We then sought to investigate how the chemical modification of the active layer caused by the HTL affects its carrier diffusion length. We designed an experiment based on the previously reported 1D donor–acceptor method.[43] In this method, incident light excites the top donor CQD layer (E_g = 1.3 eV) and the photoexcited carriers transport to the bottom acceptor CQD layer (E_g = 1.0 eV, emitter) where they recombine radiatively (**Figure 4**a). As the thickness of the donor layer is varied, the photoluminescence (PL) intensity of the acceptor layer starts to decrease past a certain thickness: fewer charge carriers reach the acceptor layer due to non-radiative recombination in the diffusive layer. By monitoring the PL intensity of the acceptor layer as a function of thickness of the donor layer, we were able to estimate the carrier diffusion length of the donor layer.

To study transport in the context of the full materials stack, we used a CQD active layer with E_g = 1.3 eV as the donor layer, and an EDT-exchanged film (E_g = 1.0 eV) or MA-exchanged film

**ADVANCED
SCIENCE NEWS**

www.advancedsciencenews.com

**ADVANCED
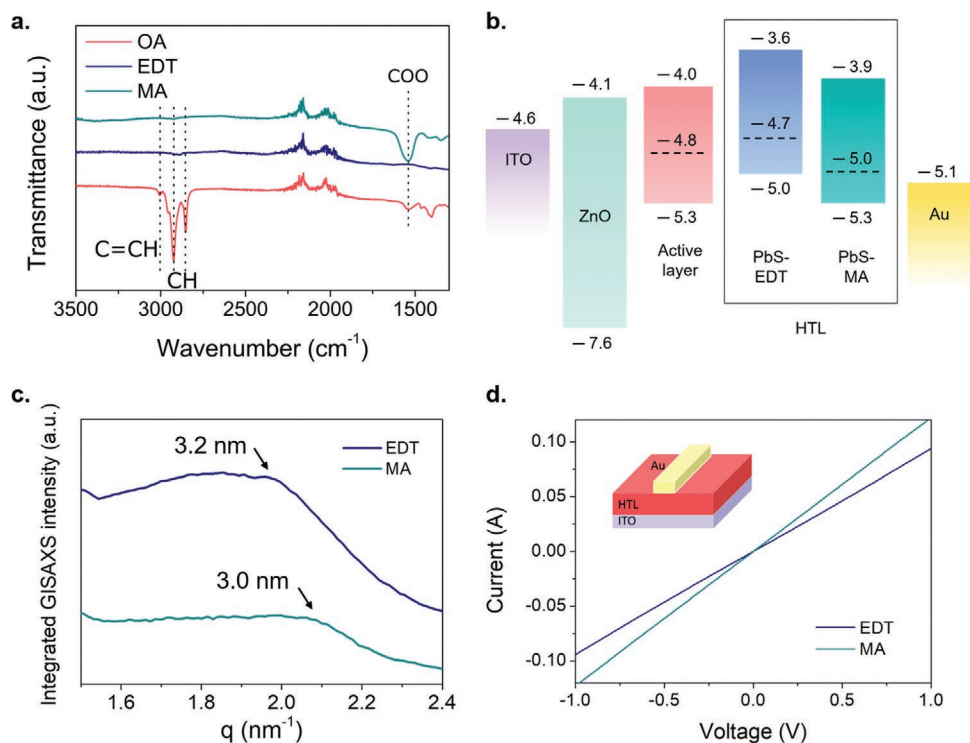MATERIALS**

www.advmat.de

Figure 3. a) Transmission FTIR spectra of OA-capped PbS CQDs before ligand exchange and after ligand exchange with EDT and MA, respectively. b) Energy levels of the full device, measured using UPS taken together with UV–vis absorbance. Top edge, dashed line, and bottom edge represent CBM, E_F, and VBM, respectively. The values used for ITO, ZnO, and Au are based on a previous report.[27] c) Integrated GISAXS intensity for PbS-EDT and PbS-MA. d) Dark I–V curve for a device with ITO/HTL ($\approx$60 nm)/Au configuration.

(E_g = 1.0 eV) as acceptor layer. The normalized PL intensity is plotted as a function of donor layer thickness (Figure 4b). In this set of experiments, we use the term effective carrier diffusion that takes into account the combined effect of the modification of the active layer and the charge transfer at the active layer/HTL. To evaluate the effective carrier diffusion length of the donor layer, we fit the data using a 1-D carrier diffusion length model.[43] Notably, although the same donor layer is used, the effective diffusion length exhibits a 1.4× increase (220 ± 10 nm;

the standard deviation is calculated based on the average of three thickness measurements) when the MA-exchanged film is used as the acceptor layer compared to that obtained when the EDT-exchanged film is used as acceptor layer (160 ± 16 nm). This result is a consequence of the preserved chemistry of the active layer and the improved charge collection efficiency at the interface.

We then pursued CQD solar cells employing the MA HTL (**Figure 5**a). The SCE profile of MA devices reveals complete charge collection at the interface between the active layer and
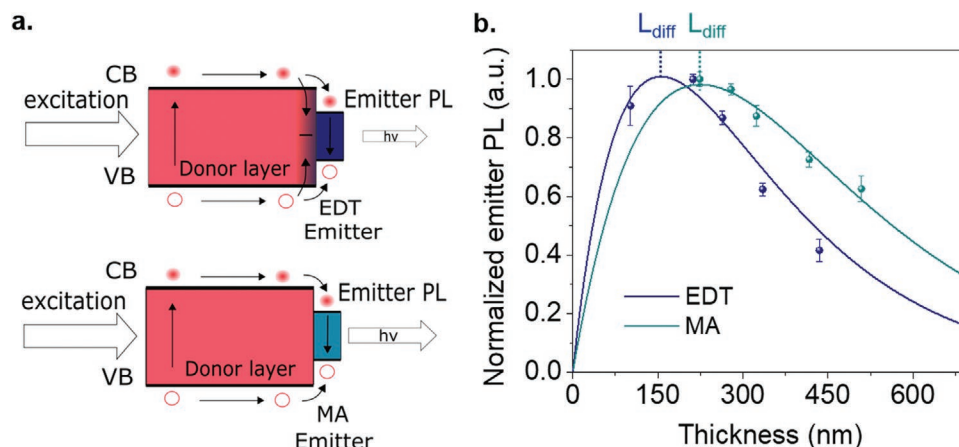

Figure 4. a) Schematics of 1D diffusion length experiments. The incident light (400 nm wavelength) excites the donor layer, and excited carriers transport to the acceptor layer (EDT emitter or MA emitter). The PL intensity from the acceptor layer is monitored. b) Normalized PL intensity to the highest signal versus thickness of the active layer for EDT devices and MA devices (dots). Fits to data based on (Equation (4) in the Experimental Section) indicate the enhancement in carrier diffusion length in the MA sample compared to the EDT sample.
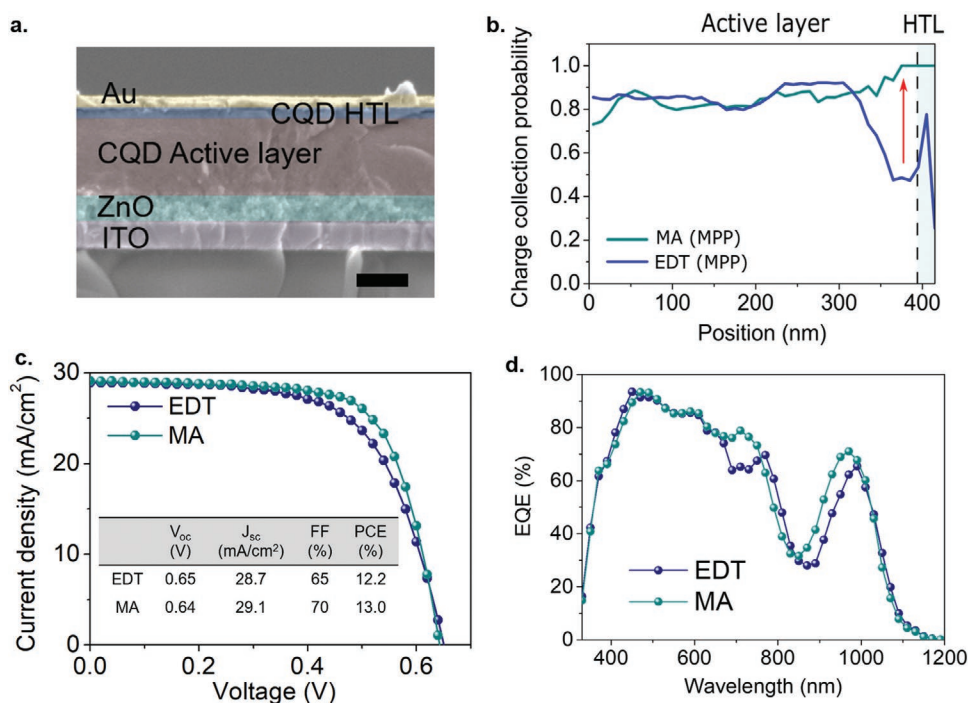
Figure 5. a) Scanning electron microscopy (SEM) cross-sectional image of full device. Scale bar = 300 nm. b) Calculated charge collection probability as a function of position in the EDT device and MA device at MPP (0.5 V). c) Experimental J–V curves for EDT and MA devices. d) Experimental EQE for EDT device and MA devices.

HTL at 0 V (Figure S9, Supporting Information). Under operating conditions at the MPP, MA devices exhibit near-unity collection efficiency at the interface. In contrast, EDT devices only collect approximately half of charge carriers near the interface (Figure 5b). As a result, the best MA devices achieve a PCE of 13.0% with an open-circuit voltage (V_{OC}) of 0.64 V, a J_{SC} of 29.1 mA cm^{-2}, and a FF of 70%, whereas EDT devices show a PCE of 12.2% (Figure 5c). Data show that this improvement by MA HTL is statistically significant (Figure S10, Supporting Information); MA and EDT devices exhibit an average PCE of 12.8 ± 0.2 % and 12.0 ± 0.2%, respectively. External quantum efficiency (EQE) spectra show that MA devices exhibit higher J_{SC} of 28.3 mA cm^{-2} compared to 27.5 mA cm^{-2} for EDT devices when the thickness of the active layer is kept the same (Figure 5d).

The most significant improvement is given by an increase in the FF value. This is a consequence of the improved collection efficiency of the devices at MPP, as seen also in SCE measurements. The improved conductivity of the MA HTL also reduces the series resistance at V_{oc} (3.9 Ω cm^{-2} for EDT devices and 2.3 Ω cm^{-2} for MA devices), contributing to the FF improvement. The MA devices also exhibit a higher optimal thickness compared to the EDT devices (Figure S11, Supporting Information), in agreement with enhanced effective diffusion length as shown in Figure 4b.

The improved SCE at the back interface leads to a redistribution of the EQE at longer wavelength region (600–1000 nm), given the higher efficiency in collecting the photons at the back of the device.

We also note that the EDT and MA devices have similar V_{oc} value. This can be explained by the fact that, as shown by UPS, the MA HTL and the EDT HTL are characterized by the same doping level, which is normally the chief cause of V_{oc} variations.[44] In order to explore the effects of a difference in energy level on device operation, we used SCAPS:[45–47] the results of the simulations (Figure S6, Supporting Information) show that the MA HTL enables increased depletion region of the active layer, in agreement with the FF and J_{sc} improvement observed in devices.

Transient photovoltage (TPV) measurements were performed in order to explore the dynamics of charge carriers in the devices. A longer TPV decay time is observed in MA devices (Figure S12, Supporting Information). This supports the findings of improved charge extraction in the MA devices which enables higher J_{sc} and FF.

The MA devices also exhibit excellent air stability, retaining 99% of their initial PCE after 80 days of storage under ambient air condition (Figure S13, Supporting Information).

In sum, this work investigated the origins of the incomplete charge collection at the active layer/HTL interface in the best prior CQD PV devices. We identified a key role for the fabrication process of the HTL, widely-used EDT ligands substitute the initial surface chemistry of the CQD active layer, a side effect of their high reactivity with the CQDs. To overcome this issue, we explored new candidate ligands with both a lower binding energy than EDT and a similar work function. We demonstrate that MA-exchanged CQD film forms chemically orthogonal HTLs, leaving the underlying active layer undiminished in its performance. This strategy achieves unity charge collection efficiency at the active layer/HTL interface, which led to an increase in PCE from 12.2% to 13.0%. This work provides better understanding to design an ideal HTL in solution-processed optoelectronics.

ADVANCED
SCIENCE NEWS

www.advancedsciencenews.com

ADVANCED
MATERIALS

www.advmat.de

Experimental Section

CQD Synthesis: OA-capped PbS CQDs with first excitonic peak at 950 nm (1.31 eV) were synthesized based on a previous report.[15] Lead(II) oxide (0.9 g), oleic acid (3 mL), and octadecene (20 mL) were mixed in a three-neck flask and heated to 120 °C under vacuum for 2 h and then filled with N_2. A stock solution, 0.24 mL of hexamethyldisilathiane dissolved in 8 mL of octadecene was then injected rapidly into the flask for PbS CQD synthesis. Then, the CQD solution was slowly cooled to room temperature. Acetone was added to precipitate the CQD solution, which was then redispersed in toluene. The CQDs were further purified twice by adding a mixture of acetone and methanol. Finally, the QDs were dissolved in octane (50 mg mL^{-1}).

MA HTL Fabrication: OA capped CQD were spin-cast on the active layer at 2500 rpm (42 × (2π) rad s^{-1}) for 10 s. The OA capped CQD were soaked with a 30 mol L^{-1} MA solution in acetonitrile for 10 s for ligand exchange with MA; the concentration is higher than the EDT exchange solution given the lower reactivity of MA with the CQDs. Then, the MA CQD film was washed three times with acetonitrile. The thickness of the MA HTL is ≈30 nm.

Synthesis of CQD Inks: To produce n-type inks, the precursor solution was prepared by dissolving lead halides (lead iodide 0.1 mol L^{-1}and lead bromide 0.02 mol L^{-1}) and NH$_4$Ac (0.055 mol L^{-1}) in dimethylformamide (DMF). A 5 mL of CQD solution dissolved in octane (7 mg mL^{-1}) was added to 5 mL of precursor solution. Then the solution was mixed vigorously for 1–2 min until CQDs were transferred to DMF phase. The CQD solution was precipitated by adding toluene and dried in vacuum. The CQDs were dissolved in butylamine for further use. To produce p-type inks, the above DMF CQD solution was further treated by adding 100 μL of cysteamine solution dissolved in DMF (0.1 mol L^{-1}) with gentle stirring.[48] Then, the CQD solution was precipitated by adding toluene and dried in vacuum. The CQDs were dissolved in butylamine for further use.

CQD Solar Cell Fabrication: The ZnO nanoparticles were synthesized using a published method.[3] The ZnO nanoparticles were spin-cast on ITO substrate at 5000 rpm (83 × (2π) rad s^{-1}) for 20 s (2 layers, ≈150 nm thickness). A blend of CQD inks (mixture of n-type CQD inks and p-type CQD inks with 1:1 ratio) was used to fabricate devices.[48] The CQD films were spin-cast (2000 rpm, 33 × (2π) rad s^{-1}) on the ZnO/ITO substrate with a concentration of 280 mg mL^{-1} of the blend CQD inks in butylamine at 2000 rpm and annealed at 70 °C for 5 min in N_2-filled glove box. Then, the MA HTL was deposited through the above protocol. For the EDT HTL, the OA capped CQDs were spin-cast (2500 rpm [42 × (2π) rad s^{-1}] for 10 s) and soaked with a 0.01 vol% EDT solution in acetonitrile for 30 s and followed by three times of washing with acetonitrile; the procedure was repeated twice. A 120 nm Au top electrode was deposited by e-beam evaporation.

Solar Cell Measurement: The active area (0.049 cm^2) was determined by the aperture placed between the devices and the AM1.5 solar simulator (Sciencetech class A). Certain commercial equipment, instruments, or materials (or suppliers, or software, etc.) are identified in this paper to foster understanding. Such identification does not imply recommendation or endorsement by the National Institute of Standards and Technology, nor does it imply that the materials or equipment identified are necessarily the best available for the purpose.

Current–voltage characteristics were measured with a Keithley 2400 source measuring unit under simulated AM1.5 illumination. Devices were tested under a continuous nitrogen flow. The *I–V* curves were scanned from −0.70 to +0.1 V at 0.02 V interval steps without wait time between voltage steps. The spectral mismatch was calibrated using a reference solar cell (Newport). EQE spectra were taken by subjecting the solar cells to chopped (220 Hz) monochromatic illumination (400 W Xe lamp passing through a monochromator and appropriate cutoff filters). Newport 818-UV and Newport 838-IR photodetectors were used to calibrate the output power. The response of the cell was measured with a Lakeshore preamplifier feeding into a Stanford Research 830 lock-in amplifier at short-circuit conditions.

Spatial Collection Efficiency Calculation: Details about the method and calculations of the SCE can be found in ref. [37]. In brief, the Fredholm integral equation is used[49,50]

$$\eta(\lambda) = \int_0^t G(z,\lambda)\phi(z)dz \qquad (1)$$

where $\eta(\lambda)$ is the IQE spectrum, t is the total thickness of the active layer, $G(z, \lambda)$ is the spectral photogeneration probability, and $\phi(z)$ is the SCE. To obtain the SCE, IQE of the devices is measured and developed the optical model of the devices using refractive index (n) and extinction coefficient (k) values of the CQD films to calculate $G(z, \lambda)$. Figures S1e and S9g, Supporting Information show the calculated $G(z, \lambda)$ of the devices with EDT HTL and MA HTL, respectively.

XPS Measurements: XPS measurements were carried out using a Thermo Scientific K-Alpha system, with a 75 eV pass energy, and binding energy steps of 0.05 eV.

FTIR Measurements: FTIR spectra were obtained using a Thermo Scientific iS50 spectral range 4600–50 cm^{-1} with ATR accessory. Samples were prepared on glass substrates.

Thickness Measurements: Thickness of CQD films for SCE and 1D diffusion length studies was measured with a thickness profilometer (Bruker, Dektak XT).

SCAPS Simulations: SCAPS software was used in order to simulate the band alignment of the device under operating conditions. The CB value calculated from UPS was used to calculate the carrier concentration for the MA HTL and EDT HTL by using the following formula:

$$\sigma = p \cdot e \cdot \mu_h \qquad (2)$$

where p is the concentration of holes, μ_h is the hole mobility, e is the elementary charge, and σ is the conductivity. The hole mobility value and the conductivity value are obtained from Figure 3d and Figure S8, Supporting Information, respectively.

UPS Measurements: A helium discharge source (HeI α, $h\nu$ = 21.22 eV) was used and the samples were kept at a take-off angle of 88°. During measurement, the sample was held at a −15 V bias relative to the spectrometer in order to efficiently collect low kinetic-energy electrons. E_F was calculated from the equation, E_F = 21.22 eV − SEC, where SEC is the secondary electron cut-off. The difference between valence band (VB) and E_F, η, was determined from the VB onset in the VB region.

GISAXS Measurements: Measurements were carried out in reflection geometry at the CMS beamline of the National Synchrotron Light Source II (NSLS II), a U.S. Department of Energy (DOE) office of the Science User Facility operated for the DOE Office of Science by Brookhaven National Laboratory. Samples were measured at a detector distance of 2.789 m using an X-ray wavelength of 0.826 Å, at 0.26° angle of incidence with respect to the substrate plane. Scattering intensity was detected by a PILATUS 2M detector. Nika software package was used to sector average the 2D GIWAXS images.[51] Data plotting was done in IGOR Pro (Wavemetrics, Inc., Lake Oswego, OR, USA).

Spectroscopic Ellipsometry: Spectroscopic ellipsometry was performed using a Horiba UVISEL Plus Extended Range ellipsometer with a 200 ms integration time, a 5nm step size and a 1 mm diameter spot size at an incident angle of 70°. Soda-lime glass slides were used as substrates for each individual material, with their back covered with cloudy adhesive type to ensure back-reflections are diffusively reflected away from the detector. Fitting was performed using Horiba's DeltaPsi2 dedicated software.

Conductivity Measurements: Conductivity measurements were performed by measuring the *I–V* characteristics of the ITO/HTL/Au devices. The slope of the curve was used to determine the conductivity through the formula

$$\sigma = \frac{L}{A \times R} \qquad (3)$$

where σ is the conductivity, L is the thickness of the device, A is the area of the device, and R is the resistance of the device (calculated from the slope of the *I–V* curve). The thickness of the devices was 60 nm and was measured with a thickness profilometer.

**ADVANCED
SCIENCE NEWS**

www.advancedsciencenews.com

**ADVANCED
MATERIALS**

www.advmat.de

1D Carrier Diffusion Length Measurements: For sample preparation, the acceptor PbS CQD layer (EDT-exchanged or MA-exchanged dots, $E_g = 1.0$ eV) was deposited on the PbS CQD active layer (donor layer, $E_g = 1.3$ eV). Samples were illuminated through the donor CQD layer side using a monochromated Xe lamp at 400 nm wavelength ($\approx$15 mW cm^{-2}). The incident light is fully absorbed in the CQD active layer due to its high absorption coefficient at 400 nm. Photoluminescence measurements were carried out using a Horiba Fluorolog time correlated single photon counting system equipped with UV–vis–NIR photomultiplier tube detectors, dual grating spectrometers. The normalized PL intensity as a function of donor CQD layer thickness is fitted using the equation[43]

$$PL_{acceptor} = -\frac{\alpha}{\alpha^2 L_d^2/\tau - 1/\tau}\left(\frac{1}{L_d}e^{-d/L_d}\frac{e^{d/L_d} - e^{-\alpha d}}{e^{-d/L_d} - e^{d/L_d}} + \alpha e^{-\alpha d} - \frac{1}{L_d}e^{d/L_d}\frac{e^{-d/L_d} - e^{-\alpha d}}{e^{d/L_d} - e^{-d/L_d}}\right)$$

(4)

where L_d is the carrier diffusion length, d is the thickness of donor CQD layer, and α is the absorption coefficient, and τ is the carrier lifetime.

Transient Photovoltage Measurements: The devices were biased with white light to reach near V_{oc} conditions and photo-excited with low power laser pulses to generate small photovoltage perturbations (ΔV kept to lower than 20 mV). Monoexponential fits to normalized traces were used to estimate the carrier lifetime at V_{oc} conditions.[52,53]

Supporting Information

Supporting Information is available from the Wiley Online Library or from the author.

Acknowledgements

Conflict of Interest

The authors declare no conflict of interest.

Keywords

[1] Y. Shirasaki, G. J. Supran, M. G. Bawendi, V. Bulović, *Nat. Photonics* **2013**, *7*, 13.

[2] L. Sun, J. J. Choi, D. Stachnik, A. C. Bartnik, B. R. Hyun, G. G. Malliaras, T. Hanrath, F. W. Wise, *Nat. Nanotechnol.* **2012**, *7*, 369.

[3] J. Lim, Y. S. Park, V. I. Klimov, *Nat. Mater.* **2018**, *17*, 42.

[4] J. Gao, S. C. Nguyen, N. D. Bronstein, A. P. Alivisatos, *ACS Photonics* **2016**, *3*, 1217.

[5] H. Lee, H.-J. Song, M. Shim, C. Lee, *Energy Environ. Sci* **2020**, *13*, 404.

[6] J. M. Luther, M. Law, M. C. Beard, Q. Song, M. O. Reese, R. J. Ellingson, A. J. Nozik, *Nano Lett.* **2008**, *8*, 3488.

[7] C. H. M. Chuang, P. R. Brown, V. Bulović, M. G. Bawendi, *Nat. Mater.* **2014**, *13*, 796.

[8] R. Azmi, H. Aqoma, W. T. Hadmojo, J. M. Yun, S. Yoon, K. Kim, Y. R. Do, S. H. Oh, S. Y. Jang, *Adv. Energy Mater.* **2016**, *6*, 1502146.

[9] C. R. Kagan, E. Lifshitz, E. H. Sargent, D. V. Talapin, *Science* **2016**, *353*, 6302.

[10] H. Aqoma, S. Y. Jang, *Energy Environ. Sci.* **2018**, *11*, 1603.

[11] K. Lu, Y. Wang, Z. Liu, L. Han, G. Shi, H. Fang, J. Chen, X. Ye, S. Chen, F. Yang, A. G. Shulga, T. Wu, M. Gu, S. Zhou, J. Fan, M. A. Loi, W. Ma, *Adv. Mater.* **2018**, *30*, e1707572.

[12] N. Kirkwood, J. O. V. Monchen, R. W. Crisp, G. Grimaldi, H. A. C. Bergstein, I. Du Fossé, W. Van Der Stam, I. Infante, A. J. Houtepen, *J. Am. Chem. Soc.* **2018**, *140*, 15712.

[13] E. M. Sanehira, A. R. Marshall, J. A. Christians, S. P. Harvey, P. N. Ciesielski, L. M. Wheeler, P. Schulz, L. Y. Lin, M. C. Beard, J. M. Luther, *Sci. Adv.* **2017**, *3*, eaao4204.

[14] W. Ahmad, J. He, Z. Liu, K. Xu, Z. Chen, X. Yang, D. Li, Y. Xia, J. Zhang, C. Chen, *Adv. Mater.* **2019**, *31*, 1.

[15] M. A. Hines, G. D. Scholes, *Adv. Mater.* **2003**, *15*, 1844.

[16] D. M. Kroupa, M. Vörös, N. P. Brawand, B. W. McNichols, E. M. Miller, J. Gu, A. J. Nozik, A. Sellinger, G. Galli, M. C. Beard, *Nat. Commun.* **2017**, *8*, 2.

[17] Y. Wang, Z. Liu, N. Huo, F. Li, M. Gu, X. Ling, Y. Zhang, K. Lu, L. Han, H. Fang, A. G. Shulga, Y. Xue, S. Zhou, F. Yang, X. Tang, J. Zheng, M. Antonietta Loi, G. Konstantatos, W. Ma, *Nat. Commun.* **2019**, *10*, 5136.

[18] D. M. Balazs, M. A. Loi, *Adv. Mater.* **2018**, *30*, 180082.

[19] J. Xu, O. Voznyy, M. Liu, A. R. Kirmani, G. Walters, R. Munir, M. Abdelsamie, A. H. Proppe, A. Sarkar, F. P. Garcia de Arquer, M. Wei, B. Sun, M. Liu, O. Ouellette, R. Quintero-Bermudez, J. Li, J. Fan, L. Quan, P. Todorovic, H. Tan, S. Hoogland, S. O. Kelley, M. Stefik, A. Amassian, E. H. Sargent, *Nat. Nanotechnol.* **2018**, *13*, 456.

[20] Y. Cao, A. Stavrinadis, T. Lasanta, D. So, G. Konstantatos, *Nat. Energy* **2016**, *1*, 16035.

[21] Y. Wang, K. Lu, L. Han, Z. Liu, G. Shi, H. Fang, S. Chen, T. Wu, F. Yang, M. Gu, S. Zhou, X. Ling, X. Tang, J. Zheng, M. A. Loi, W. Ma, *Adv. Mater.* **2018**, *30*, 1704871.

[22] J. Jean, S. Chang, P. R. Brown, J. J. Cheng, P. H. Rekemeyer, M. G. Bawendi, S. Gradečak, V. Bulovic, *Adv. Mater.* **2013**, *25*, 2790.

[23] R. Azmi, G. Seo, T. K. Ahn, S. Y. Jang, *ACS Appl. Mater. Interfaces* **2018**, *10*, 35244.

[24] H. Y. Park, I. Ryu, J. Kim, S. Jeong, S. Yim, S. Y. Jang, *J. Phys. Chem. C* **2014**, *118*, 17374.

[25] N. Sukharevska, D. Bederak, D. Dirin, M. Kovalenko, M. A. Loi, *Energy Technol.* **2019**, *9*, 1900887.

[26] F. Eisner, A. Seitkhan, Y. Han, D. Khim, E. Yengel, A. R. Kirmani, J. Xu, F. P. Garcia de Arquer, E. H. Sargent, A. Amassian, Z. Fei, M. Heeney, T. D. Anthopoulos, *Sol. RRL* **2018**, *2*, 1800076.

[27] J. Choi, J. W. Jo, F. P. Garcia de Arquer, Y. B. Zhao, B. Sun, J. Kim, M. J. Choi, S. W. Baek, A. H. Proppe, A. Seifitokaldani, D. H. Nam, P. Li, O. Ouellette, Y. Kim, O. Voznyy, S. Hoogland, S. O. Kelley, Z. H. Lu, E. H. Sargent, *Adv. Mater.* **2018**, *30*, 1801720.

[28] J. Yang, J. Lee, J. Lee, W. Yi, *ACS Appl. Mater. Interfaces* **2018**, *10*, 25311.

[29] S. Pradhan, A. Stavrinadis, S. Gupta, S. Christodoulou, G. Konstantatos, *ACS Energy Lett.* **2017**, *2*, 1444.

[30] H. Aqoma, M. Al Mubarok, W. Lee, W. T. Hadmojo, C. Park, T. K. Ahn, D. Y. Ryu, S. Y. Jang, *Adv. Energy Mater.* **2018**, *8*, 1800572.

[31] X. Zhang, Y. Justo, J. Maes, W. Walravens, J. Zhang, J. Liu, Z. Hens, E. M. J. Johansson, *J. Mater. Chem. A* **2015**, *3*, 20579.

[32] Y. Shang, H. Tang, R. Wang, X. Wu, Z. Ning, H. Chen, K. Xu, W. Zhou, *Adv. Mater.* **2018**, *30*, 1704882.

[33] D. M. Balazs, K. I. Bijlsma, H. H. Fang, D. N. Dirin, M. Döbeli, M. V. Kovalenko, M. A. Loi, *Sci. Adv.* **2017**, *3*, eaao1558.

[34] M. J. Speirs, D. M. Balazs, D. N. Dirin, M. V. Kovalenko, M. A. Loi, *Appl. Phys. Lett.* **2017**, *110*, 103904.

[35] A. G. Pattantyus-Abraham, I. J. Kramer, A. R. Barkhouse, X. Wang, G. Konstantatos, R. Debnath, L. Levina, I. Raabe, M. K. Nazeeruddin, M. Grätzel, E. H. Sargent, *ACS Nano* **2010**, *4*, 3374.

[36] A. R. Kirmani, A. D. Sheikh, M. R. Niazi, M. A. Haque, M. Liu, F. P. Garcia de Arquer, J. Xu, B. Sun, O. Voznyy, N. Gasparini, D. Baran, T. Wu, E. H. Sargent, A. Amassian, *Adv. Mater.* **2018**, *30*, 1801661.

[37] O. Ouellette, A. Lesage-Landry, B. Scheffel, S. Hoogland, F. P. García de Arquer, E. H. Sargent, *Adv. Funct. Mater.* **2019**, *30*, 1908200.

[38] F. Chen, X. Li, J. Hihath, Z. Huang, N. Tao, *J. Am. Chem. Soc.* **2006**, *128*, 15874.

[39] G. Segev, H. Dotan, D. S. Ellis, Y. Piekner, D. Klotz, J. W. Beeman, J. K. Cooper, D. A. Grave, I. D. Sharp, A. Rothschild, *Joule* **2018**, *2*, 210.

[40] A. R. Kirmani, G. H. Carey, M. Abdelsamie, B. Yan, D. Cha, L. R. Rollny, X. Cui, E. H. Sargent, A. Amassian, *Adv. Mater.* **2014**, *26*, 4717.

[41] J. M. Luther, M. Law, Q. Song, C. L. Perkins, M. C. Beard, A. J. Nozik, *ACS Nano* **2008**, *2*, 271.

[42] J. Endres, D. A. Egger, M. Kulbak, R. A. Kerner, L. Zhao, S. H. Silver, G. Hodes, B. P. Rand, D. Cahen, L. Kronik, A. Kahn, *J. Phys. Chem. Lett.* **2016**, *7*, 2722.

[43] D. Zhitomirsky, O. Voznyy, S. Hoogland, E. H. Sargent, *ACS Nano* **2013**, *7*, 5282.

[44] J. H. Song, H. Choi, Y. H. Kim, S. Jeong, *Adv. Energy Mater.* **2017**, *9*, 1700301.

[45] M. Burgelman, P. Nollet, S. Degrave, *Thin Solid Films* **2000**, *361*, 527.

[46] M. Burgelman, K. Decock, S. Khelifi, A. Abass, *Thin Solid Films* **2013**, *535*, 296.

[47] G. H. Kim, B. Walker, D. Zhitomirsky, J. Heo, S. J. Ko, J. Park, E. H. Sargent, J. Young Kim, *Nano Energy* **2015**, *13*, 491.

[48] M. J. Choi, F. P. Garcia de Arquer, A. H. Proppe, A. Seifitokaldani, J. Choi, J. Kim, S. W. Baek, M. Liu, B. Sun, M. Biondi, B. Scheffel, G. Walters, D. H. Nam, J. W. Jo, O. Ouellette, O. Voznyy, S. Hoogland, S. O. Kelley, Y. S. Jung, E. H. Sargent, *Nat. Commun.* **2020**, *11*, 103.

[49] A. H. J. Sinkkonen, J. Ruokolainen, P. Uotila, *Appl. Phys. Lett.* **1995**, *66*, 2.

[50] Y. Pang, H. Efstathiadis, D. Dwyer, M. Eisaman, in *Photovoltaic Specialist Conf.*, IEEE, Piscataway, NJ, USA **2015**.

[51] J. Ilavski, *J. Appl. Cristallogr.* **2012**, *45*, 324.

[52] L. V. Besteiro, A. O. Govorov, *J. Phys. Chem. C* **2016**, *120*, 19329.

[53] B. C. O'Regan, S. Scully, A. C. Mayer, E. Palomares, J. Durrant, *J. Phys. Chem. B* **2005**, *109*, 4616.